# Surface Observation Constrained High Frequency Coal Mine Methane Emissions in Shanxi China Reveal More Emissions than Inventories, Consistency with Satellite Inversion

Fan Lu[1], Kai Qin[1*], Jason Blake Cohen[1*], Qin He[1], Pravash Tiwari[1], Wei Hu[1], Chang Ye[1], Yanan Shan[1], Qing Xu[1], Shuo Wang[1], Qiansi Tu[2]

[1]*Jiangsu Key Laboratory of Coal-Based Greenhouse Gas Control and Utilization, School of Environment and Spatial Informatics, China University of Mining and Technology, Xuzhou, China*

[2]*School of Mechanical Engineering, Tongji University, Shanghai, China*

*Correspondence to Kai Qin (qinkai@cumt.edu.cn) and Jason Blake Cohen (jasonbc@alum.mit.edu)

**Abstract** This work focuses on Changzhi, Shanxi China, a city and surrounding rural region with one of the highest atmospheric concentrations of methane ($CH_4$) world-wide (campaign-wide minimum/mean/standard deviation/max observations: 2.0, 2.9, 1.3, and 16 ppm) due to a rapid increase in the mining, production, and use of coal over the past decade. An intensive 15-day surface observation campaign of $CH_4$ concentration is used to drive a new analytical, mass-conserving method to compute and attribute $CH_4$ emissions. Observations made in concentric circles at 1km, 3km, and 5km around a high production high gas coal mine yielded emissions of 0.73, 0.28, and 0.15 ppm $min^{-1}$ respectively. Attribution used a 2-box mass conserving model to identify the known mine's emissions from 0.042-5.3 ppm $min^{-1}$, and a previously unidentified mine's emission from 0.22-7.9 ppm $min^{-1}$. These results demonstrate the importance of simultaneously quantifying both the spatial and temporal distribution of $CH_4$ emissions to better control regional-scale $CH_4$ emissions. Results of the attribution are used in tandem with observations of boundary layer height to quantify policy-relevant emissions from the two coal mines as 6860±3520 kg $h^{-1}$ and 1010±347 kg $h^{-1}$ respectively. Both mines display a fat tail distribution, with respective 25th, median, and 75th percentile values of [1600, 3070, 10500] kg $h^{-1}$ and [755, 1090, 1420] kg $h^{-1}$. These findings are demonstrated to be higher than $CH_4$ emissions from equivalent oil and gas

30  operations in the USA, with one about double and the other similar to day-to-day

31  emissions inverted over 5-years using TROPOMI over the same region.

32  **Key Words:** *CH$_4$; Top-down emissions; Mass-conserving Model; Attribution; Mining*

33

34  **1    Introduction**

35      Emissions of methane (CH$_4$) contribute the second most to direct anthropogenic

36  longwave radiative forcing (Etminan et al., 2016; Li et al., 2022). Since CH$_4$ has a

37  lifetime from 9.5 to 12.5 years (Li et al., 2022; Prather et al., 2012), controlling CH$_4$

38  emissions can provide an opportunity to mitigate peak loading and slow the rate of net

39  global warming. Emissions from fossil fuel are one of the largest sources of

40  anthropogenic CH$_4$ (Kirschke et al., 2013; Saunois et al., 2020a). Since China is the

41  world's largest producer and consumer of coal (Bournazian, 2016), Coal mines

42  contribute up to 33%-40%  of China's CH$_4$ emissions (Janssens-Maenhout et al., 2017;

43  Miller et al., 2019; Peng et al., 2016). Although China enacted coal mines CH$_4$ (CMM)

44  regulations in 2010, CMM continues grow (Kerr and Yang, 2009; Miller et al., 2019).

45  CH$_4$ emission estimates remain exist uncertain in both space and time (Brandt et al.,

46  2014; Saunois et al., 2020b). They also generally have a fat tail distribution, wherein a

47  small number of samples have extremely large emissions that overwhelm emissions

48  under average conditions (Duren et al., 2019; Plant et al., 2022). For these reasons, new

49  approaches to quantify, reduce uncertainty, and attribute CH$_4$ emissions are necessary

50  and can provide support for policies aiming to control and mitigate CMM (Cao, 2017).

51      Bottom-up (BU) quantification of emissions requires a priori knowledge of source

52  locations and diversity, which tends to not represent real-world conditions. Top-down

53  (TD) approaches analyze concentration data with improving accuracy (Allen, 2014;

54  Rigby et al., 2019; Varon et al., 2018; Vaughn et al., 2018), specifically combining

55  surface (Heerah et al., 2021; Katzenstein et al., 2003; Shi et al., 2023), aircraft (Karion

56  et al., 2013; Shi et al., 2022; Tong et al., 2023; Vinković et al., 2022), and/or satellite

57  (Wecht et al., 2014) CH$_4$ observations with atmospheric models. Some TD approaches

58  use physically realistic but complex chemical transport models (Bloom et al., 2017) ,

59  others use plume models (Goldsmith et al., 2012), and others still use data driven

approaches (Buchwitz et al., 2017). Uncertainties in whether or not to consider the basic formulation of plume models as being reasonable under the observed conditions are rarely addressed holistically or in detail, including but not limited to: stable wind speed and direction (Varon et al., 2018), no outside sources intersecting the plume (Varon et al., 2018), no significant enhancement in the background concentrations (Irakulis-Loitxate et al., 2021), no pooling or other non-linear behavior within the plume (Bruno et al., 2024), or where to draw the boundaries of a plume (He et al., 2024). Similarly, large-scale chemical transport models tend to be quite stiff, with internal parameters and processes not being variable, even if on the subgrid scale this may introduce considerable uncertainty (Cohen and Prinn, 2011, Cohen and Wang 2014, Qin et al 2013; Hu et al., 2024; Lu et al., 2024).

Airborne remote sensing is a highly technical and costly approach to record $CH_4$ fluxes from landfills, coal basins, and oil and gas production (Krautwurst et al., 2021; Krautwurst et al., 2017; Kuhlmann et al., 2023), which suffers from not being able to monitor $CH_4$ emissions over long periods of time or in regions where the source is not well constrained (Brandt et al., 2014; Gorchov Negron et al., 2020; Hiller et al., 2014; Mehrotra et al., 2017; Molina et al., 2010). Satellite remote sensing can measure $CH_4$ under specific orbits where the source is known and identified (Jacob et al., 2016; Jacob et al., 2022; Plant et al., 2022; Varon et al., 2018; Zhang et al., 2020), but only after being calibrated by upward looking remotely sensed measurements (Tu et al., 2022), and only when the atmosphere is rain, cloud and aerosol free (Cohen and Prinn, 2011; Reuter et al., 2019; Sadavarte et al., 2021). TROPOMI and GOSAT have both been shown to be data-rich at times (Butz et al., 2012; Hu et al., 2018; Jacob et al., 2016), but severely limited at other times (Butz et al., 2012; Kuze et al., 2009). Even when these satellites have sufficient data to compute emissions from other species, frequently $CH_4$ emissions cannot be computed (Li et al., 2023; Qin et al., 2023b) due to insufficient signal strength, and uncertainties which are both non-understood and mis-constrained (Povey and Grainger, 2015).

88    Ground-based remote sensing provides higher accuracy versus satellite

89    observations (Heerah et al., 2021; Luther et al., 2022; Tu et al., 2022). EM27/SUN

90    measurements have approximated $CH_4$ emissions in Poland (Luther et al., 2019; Luther

91    et al., 2022). However, these instruments are expensive, require calibration, and have

92    limited data collection due to solar signal strength.

93    This work employs a high-frequency surface-based observation platform of $CH_4$

94    concentration which is portable, economical, and unaffected by most environmental

95    factors. The observations are combined with a new mass-conserving methodology

96    based on temporal transformation of the spatially derived mass-conserving framework

97    successfully applied to $NO_2$ (Li et al., 2023; Qin et al., 2023b). This work focuses on

98    Shanxi, one of the densest coal mining regions in the world, accounting for

99    approximately 10% total global coal production (Lin and Liu, 2010; Qin et al., 2023a).

100   Continuous observations were made around known coal mines, unknown sources, and

101   of background conditions. The 2-box model used the high-frequency emissions

102   calculated using these data to drive for attributing emissions to the known mine and a

103   second low production mine previously thought insignificant. The results provide

104   insights into the spatial distribution of $CH_4$ emissions, demonstrate rapid adoption of

105   practical methods globally, and enable source attribution.

106   **2   Method and Data**

107   **2.1 Study Site and Campaign Design**

108   Changzhi, Shanxi is located in a basin, with coal mines and associated coal use

109   industries densely distributed throughout both flat central regions and around the

110   mountainous edges (Figure 1), many of which are classified as high $CH_4$ emitting mines.

111   Due to this combination, city-wide background $CH_4$ concentrations are very high and

112   have large variation in time. Due to this combination, province-wide background $CH_4$

113   concentrations are very high and have large variation in time. This study mainly focuses

114   on two coal mines: one mine is classified as having high amounts of $CH_4$ emissions per

115   unit of production and an annual coal production of 4 million tons (CM-A), and the

116   other is unclassified for $CH_4$ emissions per unit of production and having an annual coal

117   production of 3 million tons (CM-B) (Qin et al., 2023a). Instruments were positioned

along concentric circles located 1km, 3km, and 5km from CM-A, over an approximation of the four ordinal directions: east, west, south, north (Figure 2). All locations were planned to be far away from known anthropogenic sources, leading to a net total 12 measurement points. As later discovered, CM-B is located approximately 1km southwest from the measurement point located at 5km west.
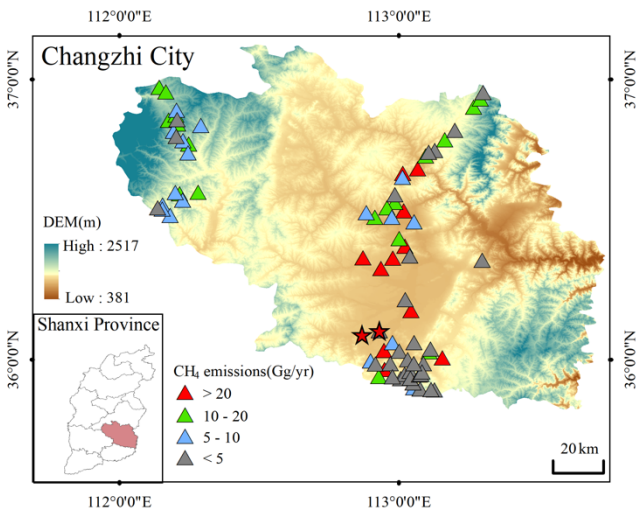
**Figure 1. Topographic map of Changzhi, and its location in Shanxi Province (bottom left). The triangles represent the locations of all individual coal mines (including underground and abandoned mines), where the triangle color represents the emissions amount: high (red), middle (green), low (blue), and very-low (grey). The red stars represent the two coal mines in this work.**
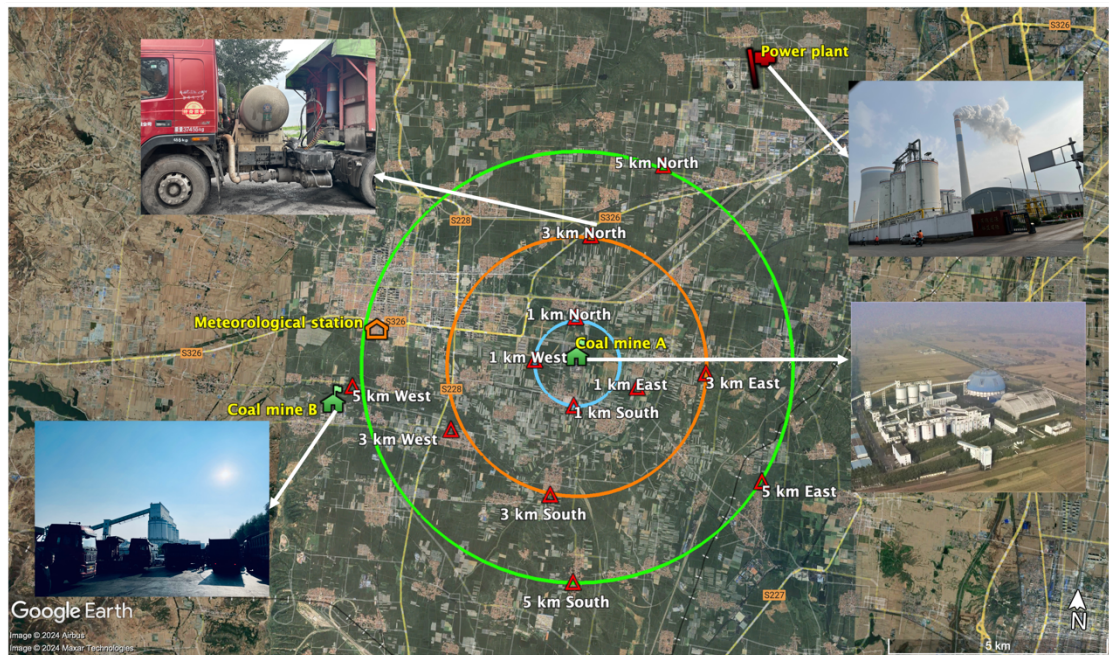
**Figure 2. Locations of four individual coal mines (Green filled houses), a power plant (Red flag), and the 12 observation locations presented in this work (red double-outlined triangles). Distance from CM-A are given as concentric circles at 1km (blue), 3km (orange), and 5km (green).**

## 2.2 Measuring CH$_4$ Concentration

Atmospheric CH$_4$ concentrations at 5 m above the surface were observed daily at 1 Hz from 8:30 to 17:00 local time in August 2022 using two portable greenhouse gas analyzers (LGR-915-0011, California, USA). Three different locations (1 km, 3 km and 5 km) were selected daily along a single direction from the CM-A, allowing a more consistent and precise calculation of the spatial gradient (Table S1). In order to reduce the time errors, using two portable greenhouse gas analyzers randomly selecting the three observation points during the daily measurements and without fixed sequence. During field experiments, each day in a background location we confirmed that the standard baseline was found within its reliable range. Further, to ensure measurement consistency when the instrument's location was changed, after relocation, we rechecked the condition against the standard baseline. Another, the instrument was allowed to stabilize and any air from the previous location was flushed out, with the first 10 minutes of measurement data discarded, to ensure that only local air was observed.

The CH$_4$ concentrations data was averaged minute-by-minute to match observed wind data, and subsequently used to compute CH$_4$ emissions. As show in Figure S1 and S2, the CH$_4$ concentrations data is highly correlated with rapid changes in both the wind speed and direction.

Observations made in clean locations with a wind direction not from the mine are subsequently considered for background sites. The lowest and least variable CH$_4$ concentrations observations are found on August 23 in the south (2.08±0.08 ppm) (Figure S2). It is important to note that although this site has the minimum concentrations observed in this work, these values are significantly higher than the global latitude-band background. Three other locations and days were observed with relatively low mean and not significantly large variation: August 19 in the east (2.63±0.35 ppm), August 22 in the east (2.65±0.51 ppm) (Figure S1), and August 22 in the south (2.60±0.55 ppm) (Figure S2). These results highlight the importance of accurately determining background concentrations in mass-balance emissions estimates. Unlike satellite-based emissions assessments, which often rely on separating plumes from global latitude bands or climatological background states (Buchwitz et al.,

2017; Irakulis-Loitxate et al., 2021; Lauvaux et al., 2022; Sadavarte et al., 2021), in situ measurements typically determine background concentrations by sampling upwind or outside the plume (Brantley et al. 2014). In this study, we have taken the spirit of the latter approach a step further, to ensure that concentrations observed as relatively clean are actually representative of locally background air. This way ensures that our background concentrations were representative of the local conditions not influenced directly by the site of interest (Figure S2). This method provides a more accurate approach when the baseline itself also changes, as in the specific locations sampled in this work.

**2.3 Meteorological Data**

The wind speed and direction were obtained from local meteorological stations with a temporal frequency of 1min. As show in Figures 3 and 4 the overall wind was dominated by a southerly direction (38.0% of observations between 150° and 210°) and found to be moderately slow (69.9% of observations were between 1 m s$^{-1}$ and 4 m s$^{-1}$). The 10$^{th}$ and 90$^{th}$ percentiles of wind direction (54° and 312°) and wind speed (1 m s$^{-1}$ and 5.1 m s$^{-1}$) respectively, indicate that high frequency sampling reveals a small number of relatively large changes are observed, which are expected to lead to a "fat-tail" type of distribution of subsequently computed CH$_4$ emissions (Delkash et al., 2016).

The temperature and pressure data were measured by a handheld meteorological instrument (HWS1000, ZOGLAB, China) with an ccuracy of ± 0.5 °C for temperature and ± 0.5 hPa for pressure, ensuring reliable data collection. The meteorological instrument was calibrated according to the manufacturer's guidelines prior to use. Measurements were taken at 5 s intervals to capture temporal variations in the atmospheric conditions. The temperature and pressure data were averaged minute-by-minute to match observed wind data, and subsequently used to convert CH$_4$ emissions unit (ppm min$^{-1}$) into policy-relevant unit (kg h$^{-1}$).The boundary layer data were obtained from https://zenodo.org/records/6498004 (Guo et al., 2022) based on a merging of reanalysis data with observations (Guo et al., 2024).

191
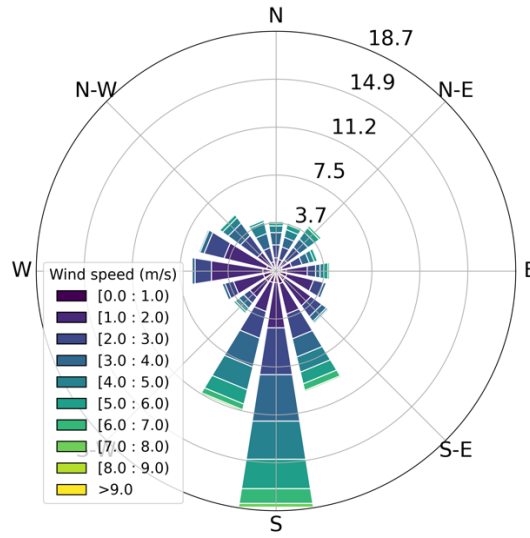
192 **Figure 3. The wind rose of all observed wind speeds from August 10, 2022 to August 25, 2022.**

193
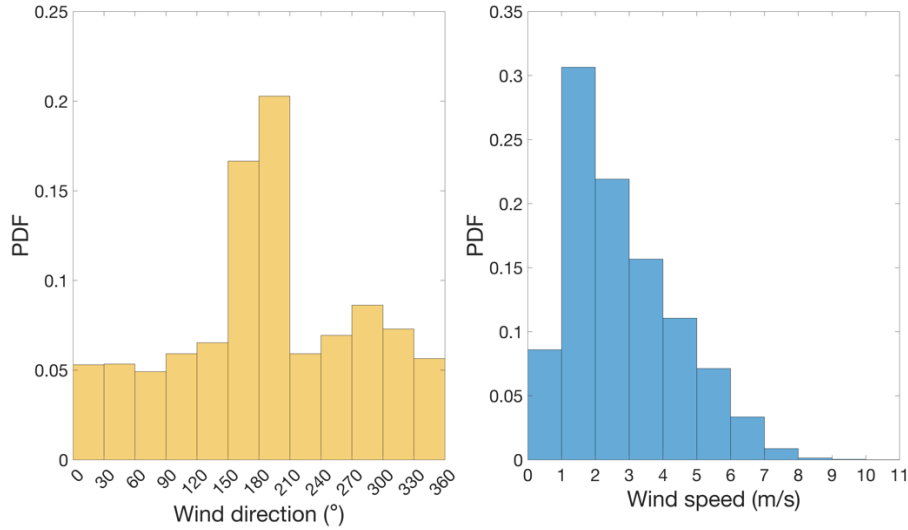
194 **Figure 4. Probability density function (PDF) for all observed wind direction (yellow) and wind speed (blue)**

195 **from August 10, 2022 to August 25, 2022.**

196 **2.4 Quantitative Estimation of $CH_4$ Emissions**

197     A mass conserving approach was used to estimate the $CH_4$ emissions using high

198 frequency observations of $CH_4$ concentrations and meteorological data, hereafter called

199 the Mass Conserving Model of Measured CMM ($MCM^2$). This approach is based on

200 previous dynamic emissions estimates of tropospheric atmospheric column

201 observations of short-lived $NO_2$ (Li et al., 2023; Qin et al., 2023b), and $CH_4$ (Hu et al.,

202 2024) but has never been applied to surface observations or at minute-frequency scale.

203 Adopting this approach to solve for $CH_4$ emissions is done starting with the continuity

204 equation for the conservation of mass (Equation 1), reorganizing the individual terms

205 and converting coordinates from space to time (Equation 2) and finally combining the

206 terms (Equation 3) as follows:

207
$$\frac{\partial [CH_4]}{\partial t} = ECH_4 - \nabla(U \times [CH_4]) \qquad (1)$$

$$\nabla(U \times [CH_4]) = [CH_4] \times \nabla U + U \times \nabla[CH_4]$$

$$= \alpha \times \left([CH_4] \times \frac{\partial U}{\partial t} + U \times \frac{\partial [CH_4]}{\partial t}\right) \quad (2)$$

$$\frac{\partial [CH_4]}{\partial t} = ECH_4 - \alpha \times \left([CH_4] \times \frac{\partial U}{\partial t} + U \times \frac{\partial [CH_4]}{\partial t}\right) \quad (3)$$

where $[CH_4]$ is the $CH_4$ concentration (ppm), $\frac{\partial}{\partial t}$ is the temporal derivative operator, $ECH_4$ is the $CH_4$ emissions flux (ppm min$^{-1}$), U is the wind speed (m s$^{-1}$), and the $\nabla$ is a mathematical o gradient operator acting on spatially distributed variables. However, when considering motion along one-dimension, the relationship between distance, speed, and time can be used to rewrite the spatial derivatives of $\nabla([CH_4])$ and $\nabla(U)$ as temporal derivatives (Brasseur and Jacob, 2017), where $\alpha$ is a conversion coefficient between distance and wind speed.

The gradient term used in these equations take into account the local topography of Shanxi, which is known for its significant features and surrounding mountains. These geographical features can impact the transport and dispersion of $CH_4$, and their effects are incorporated into the wind field in the continuity equation. Notably, when dealing with a non-divergent wind field, the gradient term simplifies to the term $(U \times \nabla[CH_4])$ (Sun, 2022). Uncertainty analysis was conducted before calculating the $CH_4$ emissions to ensure only reliable data was used, since observed variation of $CH_4$ concentrations over time is influenced not only by $CH_4$ emissions, but also changes in wind speed and pressure. Specifically, $[CH_4] \times \frac{\partial U}{\partial t}$ represents the change in $CH_4$ concentrations influenced by pressure, while $U \times \frac{\partial [CH_4]}{\partial t}$ represents the change in $CH_4$ concentrations influenced by advection. Furthermore, since there is uncertainty in the observations, this work takes a conservative approach, and only considers data when the threshold given by equation (4) is observed to be considered influenced by emissions ( a lower threshold can be selected like 25% or 15% et al., but uncertainty will increase).

$$U \times \frac{\partial [CH_4]}{\partial t} / \nabla(U \times [CH_4]) > 30\% \quad (4)$$

The remaining data (approximately 22%, presented as red circle indicators in Figure 5) is not processed in the emissions calculation as the signal is most likely due to a combination of observational uncertainty and white noise (Prinn et al., 1987; Conrad et al., 2023).
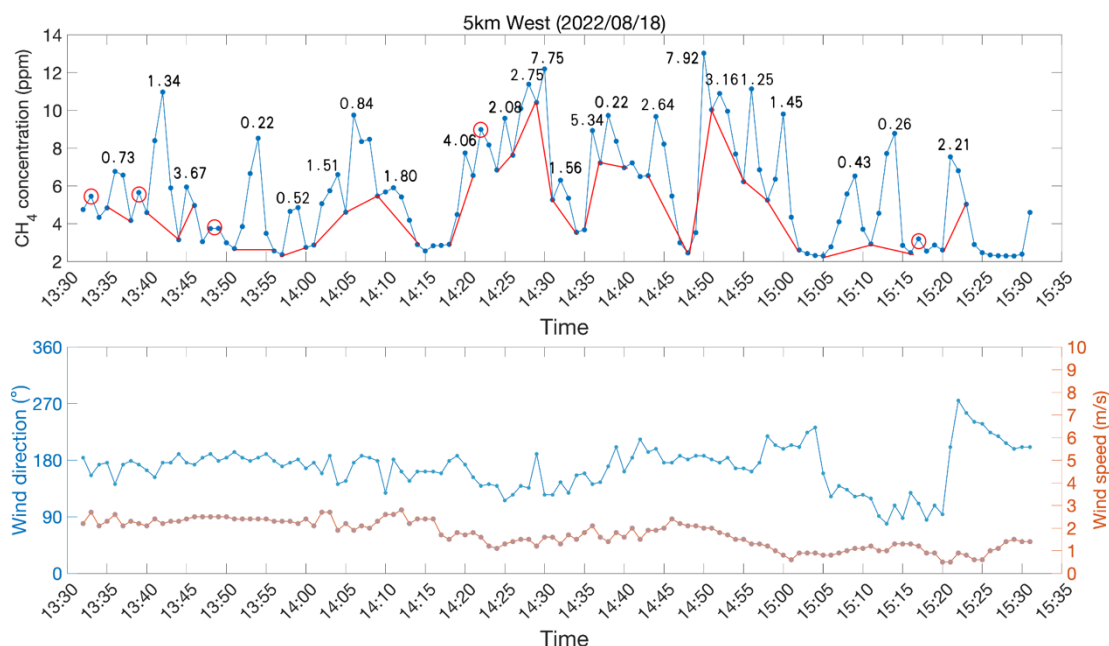
**Figure 5. Time series of CH$_4$ concentrations (top, blue), background concentrations (top, red), wind direction (bottom, blue) and wind speed (bottom, red) measured 5km west of CM-A on August 18, 2022. MCM$^2$ computed CH$_4$ emissions (top, numbers) (ppm min$^{-1}$) are computed for all regions where the observations are enhanced compared with the background for at least 3 consecutive observations, and which further pass the noise threshold (Equation 4).**

## 2.5 Uncertainty Analysis

In order to reduce the uncertainty of the CH$_4$ emissions estimation, only data above the threshold given by equation (4) is consided. Prior to this, uncertainty analysis was also conducted on the relevant variables in actual experiments. As shown in Figure 6, a 5% uncertainty was assigned to both the CH$_4$ concentrations and wind speed data, and the CH$_4$ emissions was calculated. The uncertainty analysis results indicate that probability distribution of all possible calculated emissions are consistent, and the errors are smaller than 5% in each case, consistent with Equation 3 leading to a dampening of the uncertainty, as also observed in Qin et al. (2023a) study. Therefore, we believe that the results of CH$_4$ emissions in this study can be trusted.
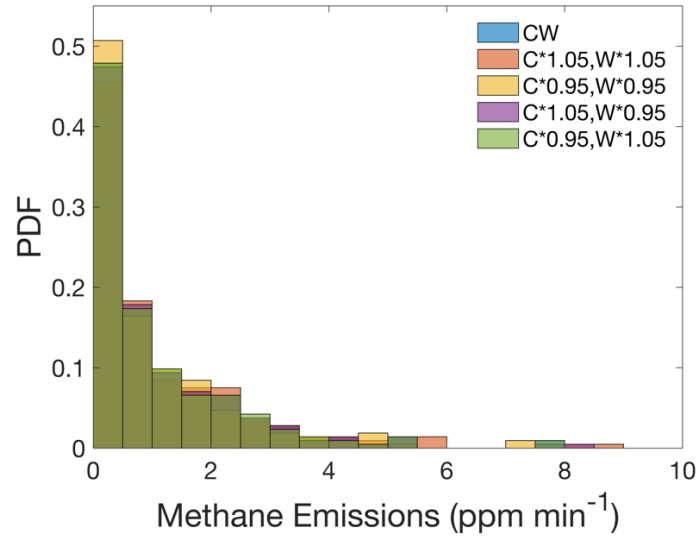
Figure 6. The PDFs of uncertain analysis results (C represents CH₄ concentrations, W represents wind speed).

**2.6 Attribution Analysis**

A 2-box mass conserving model (based on equation 5) was used to attribute $CH_4$ emissions from the more than one suspected source of $CH_4$ emissions in the 5k west. An overview of the MCM[2] and 2-box mass comserving model used in this work is provided in Figure 7. The changes in $CH_4$ concentrations ($C_{coal\ mine}$ (ppm)) over time t (min) at the observation point is driven by $CH_4$ emissions ($E_{coal\ mine}$ (ppm min⁻¹)) from the upwind coal mine and the $CH_4$ concentration blown away from the coal mine by the wind U (m s⁻¹), and the $CH_4$ background concentration ($C_{background}$ (ppm)) as demonstrated in Figure 7.

$$\frac{\partial C_{coal\ mine}}{\partial t} = E_{coal\ mine} + U \times C_{background} - U \times C_{coal\ mine} \qquad (5)$$

All observed $CH_4$ concentrations data and estimated $CH_4$ emissions data are used when wind direction is capable of transporting the $CH_4$ from either CM-A or CM-B towards the observation site (Figure 10), while the remaining data is not used. A discretized version of Equation 5 is given in Equation 6 and solved using a first order finite difference approach:

$$C_{Coal\ mine_{\tau i+1}} - C_{coal\ mine_{\tau i}} = E_{coal\ mine_{\tau i}} + U_{\tau i} \times C_{background_{\tau i}} - $$

$$U_{\tau i} \times C_{coal\ mine_{\tau i}} \qquad (6)$$

where $\tau_i$ and $\tau_{i+1}$ are the current and next time step, and the other terms are defined as in equation 5.

274    All possible sets of steady-state CH$_4$ concentrations are computed using all
275    possible combinations of CH$_4$ emissions and observed CH$_4$ concentrations as boundary
276    and initial conditions and running the equation forward to equilibrium.

277    The analyze probabilistically by comparing the modeled CH$_4$ concentrations
278    probability density function (PDF) with the observed CH$_4$ concentrations PDF.
279    Differences between the PDFs are clearly associated with the different wind directions
280    and hence geophysical locations of the CH$_4$ emissions sources can be distinguished.
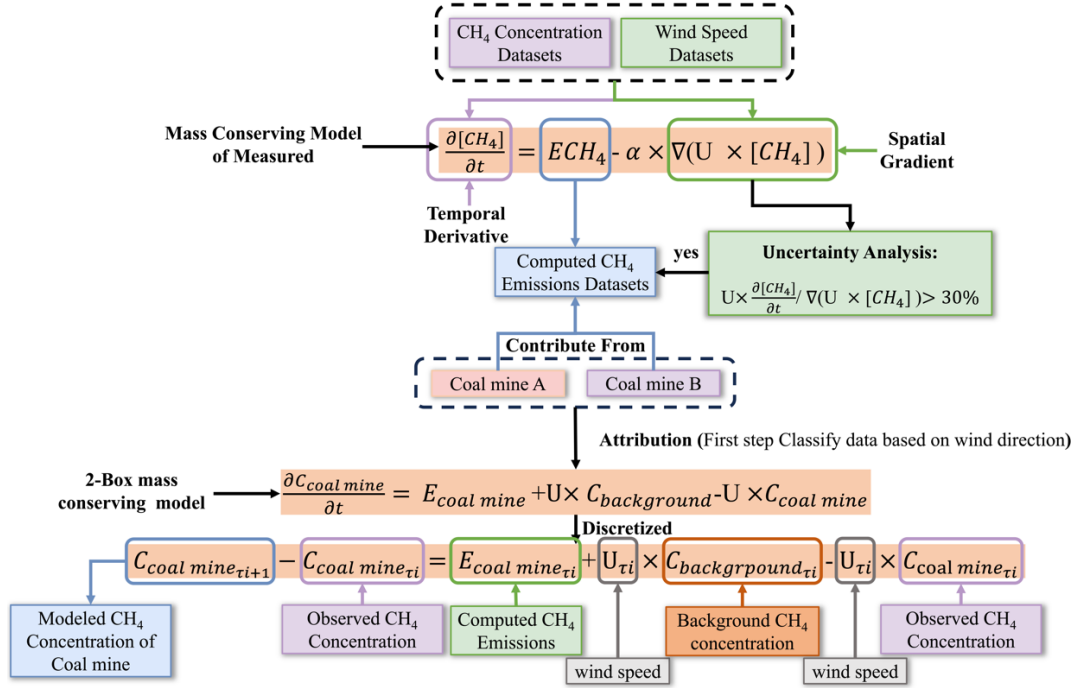
281
282    **Figure 7. Overview of the MCM2 and 2-box mass conserving model used in this work.**

283
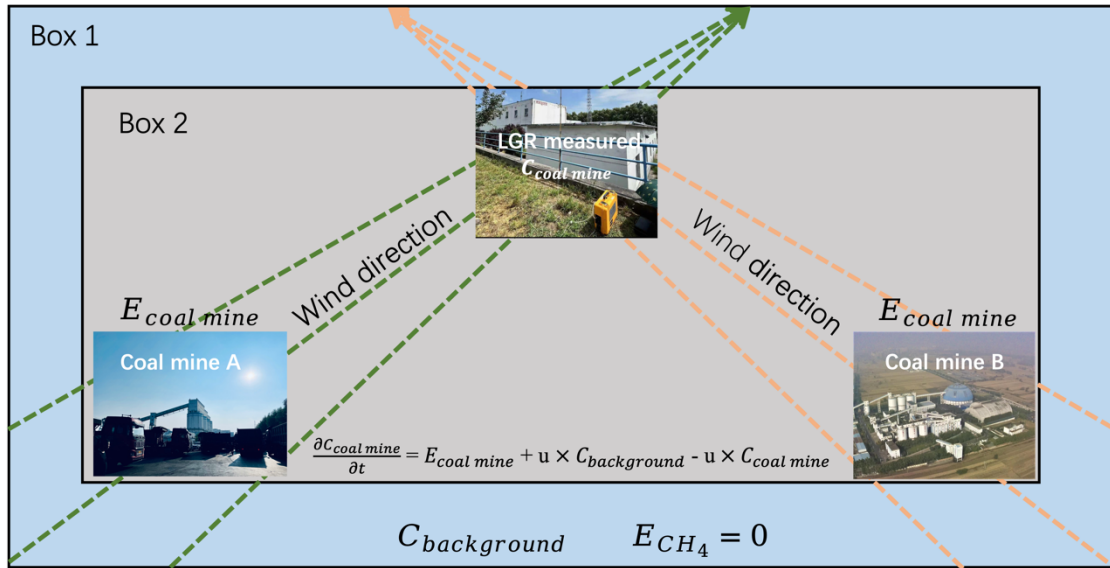
284    **Figure 8. Schematic diagram of the 2-Box model.**

285    **2.7 Converting Emissions into Policy-Relevant Units**

286        In order to compare the emissions with some other studies, the units (ppm min^{-1})
287    were converted into policy-relevant units (kg h^{-1}), although as outlined below, this
288    conversion leads to a larger uncertainty range. According to the attribution analysis in
289    Section 2.6, when the wind direction is located within a 60° arc of coal mine A or coal
290    mine B (Figure 8), the respective $CH_4$ emissions which successfully passed attribution
291    were assigned to the respective coal mine. Therefore, based on the wind direction, the
292    $CH_4$ emissions of coal mine A reported in this study use all of the data from the north 1
293    km $CH_4$ station, the $CH_4$ emissions of coal mine B considered all of the data from the
294    west 5 km $CH_4$ station, and the background data came from all of the non-emissions
295    data.. adopting the following equation (7) to converte the units from ppm min^{-1} to kg h[-
296    [1]:

$$E'CH_4 = ECH_4 \times \rho_{air} \times H \times A \times 60 \quad (7)$$

$$\rho_{air} = \frac{P \times M_{air}}{R \times T} \quad (8)$$

299    Where $E'CH_4$ is the $CH_4$ emissions with unit of kg h^{-1}, $ECH_4$ is the $CH_4$ emissions with

300    unit of ppm min^{-1}, $\rho_{air}$ is the dry gas density (kg m[3]) (based on equation 8), H is the

301    height of the vertical rise that the emissions undergo within their first minute (m), A is

302    the area (m[2]) swept over an arc (Figure 9), which ranges linearly from 60° under slow

303    wind conditions to 30° over very fast wind conditions, based on the wind speed when

304    the direction is found to lead to successful attribution. P is the atmosphere pressure (Pa)

305    over the sampling duration, $M_{air}$ is the molecular weight of dry air, which is a fixed

306    constant (28.97×10^{-3} kg mol^{-1}), R is the universal gas constant (8.314J mol^{-1} k[-1]), T is

307    the air temperature (K) over the sampling duration.

Hight: V×T    Bottom area: $\pi \times R^2 \times \frac{1}{6}$

V: Vertical wind speed, assuming the vertical wind speed is 1/10 horizontal wind speed here

T: Observation/calculated integration time for methane emissions, between 3 minutes to 8 minutes in this work

R: Radius of a circle, the distance transmitted by the horizontal wind speed during the integration time used to calculate each methane emission

308

309    **Figure 9. The control volume for CH$_4$ emissions unit convertion from ppm min$^{-1}$ to kg h$^{-1}$.**

310    Two different assumptions are made for the vertical extent of the plume rise, since the emissions are

311    computed minute-by-minute which is shorter than the adjustment time throughout the entire boundary

312    layer (Vaughn et al., 2018; Zinchenko et al., 2002). The first is to assume it has mixed within the bottom

313    one fourth of the boundary layer, and the second is that it has mixed based on a steady vertical rise equal

314    to one tenth of the horizontal wind. In this work, results using both assumptions will be presented.

315    **3    Results and Discussion**

316    **3.1 Spatial Distribution Characteristics of CH$_4$ Concentration Around Coal Mine**

317    Time series of CH$_4$ concentration, wind speed, and direction at 1 km, 3 km and 5

318    km north of CM-A are given in Figure 10. The wind direction predominantly blew from

319    CM-A towards the observation point (wind direction is between 150° and 210°), for

320    about 60% of the daily observation time.  Only one day (August 15) observed at 1km

321    north with a significant amount of wind from the west (wind direction is between 240°

and 300°), accounting for approximately 92.8% of the observation time on that day. Consistent with CM-A being the major source at 1km, when the wind blew from the south, the $CH_4$ concentration (3.45±0.79 ppm) was both higher and had a larger variation than when the wind blew from the west (2.40±0.17 ppm) which was similar to background conditions. This is consistent with there being no known significant sources to the west from this observation location, as shown in Figure 2. Similarly, under faster than average wind conditions from the direction of CM-A (on August 21 the mean wind was 5.70 m s$^{-1}$ with 14.9% of observations faster than 7 m s$^{-1}$), the observed $CH_4$ concentrations were slightly lower, yet similarly variable (3.17±0.82 ppm). All of these findings are consistent with transport dominating the $CH_4$ concentrations at 1 km north, and that high frequency wind and $CH_4$ concentration observations are required in tandem to compute the required spatial gradients in the $CH_4$ emissions, otherwise there is no basis to objectively separate the effects of the emitting region (CM-A) from the background.
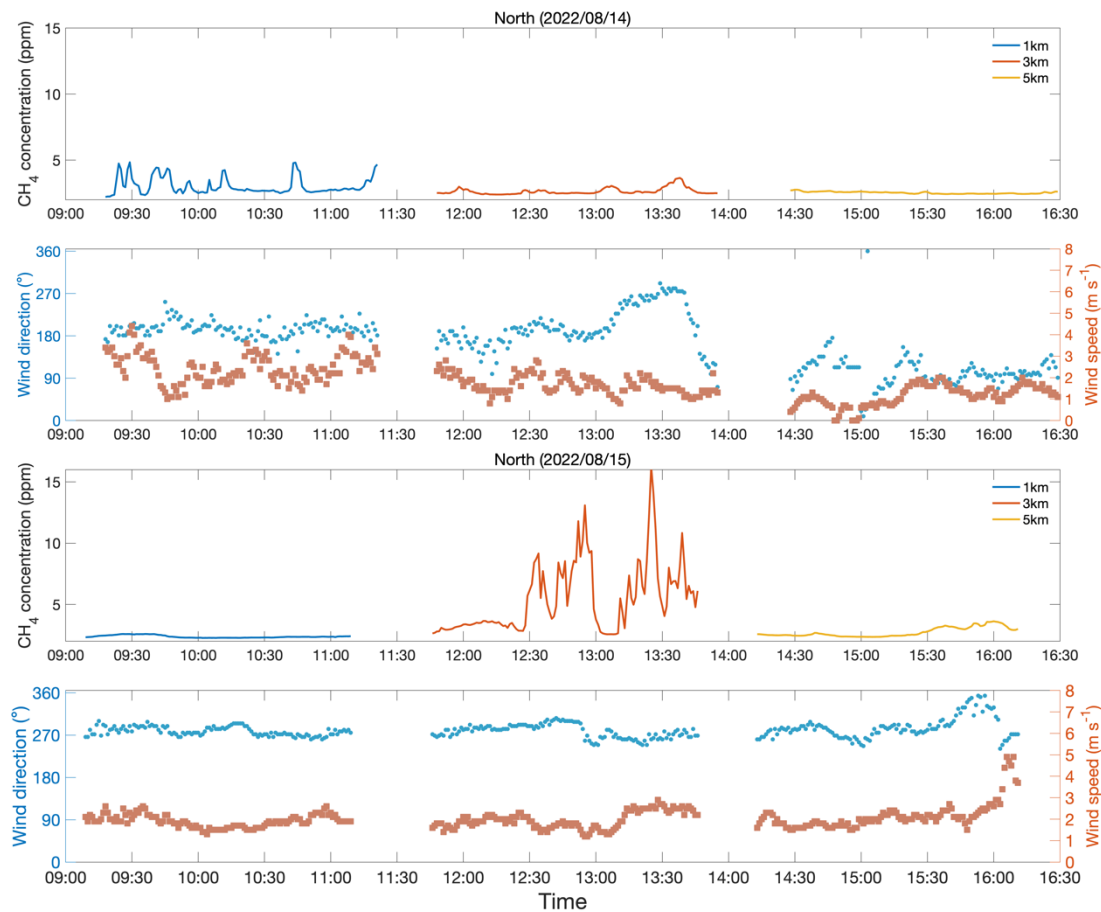
**Figure 11. Time series of CH$_4$ concentrations (ppm), wind speed (m s$^{-1}$) and wind direction (º) measured at 1km (blue line), 3km (red line) and 5km (yellow line) located north of CM-A on two different days.**

A similar set of findings were observed at 3 km north, while 5 km north is generally similar to the CH$_4$ background concentrations. At 3 km north, when the wind was from the south (59.3% of data), the CH$_4$ concentration was lower and more variable (3.16±1.48 ppm, with 78.7% of observations below 3.0 ppm) than at 1 km north, consistent with advection from CM-A and a relatively stable atmosphere with a small contribution from diffusion between the plume and the background. When the wind blew from other directions, the distribution of CH$_4$ concentrations broadened considerably, with a range from background (2.25 ppm) through extremely polluted (16.2 ppm). One subset of this was observed on August 15 (observed over a total of 61 mins of observations, 6.68% of the total observations at 3 km north) when the wind was

from the west and slow, where the $CH_4$ concentration was (5.44±2.82 ppm), as depicted in Figure 10. The data on this day aligned with the presence of a major highway west of the observation site, which was observed in-person to have heavy traffic consisting of vehicles carrying coal (which could still be outgassing) as well as others powered by compressed natural gas (CNG) (Figure 2). At 5 km north the overall $CH_4$ concentrations (2.40±0.28 ppm) was generally lower than at 3km and had much lower variability, consistent with background $CH_4$.

Time series of $CH_4$ concentrations measured at 1 km, 3 km and 5 km west of CM-A and corresponding wind direction and speed are given in Figure 11. Overall, the main wind direction is from the south 98.4% of the time at 1km, 74.5% of the time at 3km, and 70.2% of the time at 5 km, and the wind speed was very high when measuring $CH_4$ at 1 km west, with an average value of 4.28±1.13 m s$^{-1}$ and a maximum of 7.4 m s$^{-1}$. This set of findings is consistent with clean upwind sources. Accordingly at 1km west, the observed $CH_4$ concentrations were slightly higher than $CH_4$ background concentrations and had similar variability to 1km and 3km north (2.71±0.94 ppm and 86.5% of the data below 3 ppm). At 3 km west, $CH_4$ concentrations was observed to be similar to the $CH_4$ background concentrations (2.32±0.09 ppm). The only exception was found at 1 km west between 9:00 am and 9:30 am on August 17, in which all of the observations of $CH_4$ concentrations were greater than 4 ppm. Since the areas to the west from 1 km west contains mostly farmland, there was no expected strong sources of $CH_4$, as shown in Figure 2. This indicates that during this special short time, the observed slow increase and rapid fall-off in $CH_4$ concentrations must be due an unidentified sources, or a change in the boundary layer or vertical mixing structure.

Following this, it was anticipated that the 5 km west site would exhibit background types of conditions, however the observed data deviates significantly. Wind speed was low (1.63±0.54 m s$^{-1}$, maximum 3.0 m s$^{-1}$), $CH_4$ concentrations were both very high and exhibited substantial temporal variability (5.83±2.99 ppm, 66.7% of $CH_4$ concentrations data exceeding 4 ppm, and peak of 15.3 ppm), and 70.2% of the $CH_4$ concentrations observations were from the south as demonstrated in Figure 12d,e,f. From Figure 1, it can be seen that there is another coal mine (CM-B) located about 1

km away from the 5 km west measurement point, to its southwest, although CM-B has an annual production of about 3 million tons (smaller than CM-A) and not considered to be high gas (like CM-A), and therefore was not previously considered important. The overlap of high $CH_4$ concentrations with low a priori emissions, suggests that formal attribution is essential to quantitatively confirm whether CM-B is the source responsible for both typical conditions at 5 km west, as well as the long-range transport event at 1 km west.

CH$_4$ concentrations and wind observations in all directions except to the west, and except for the small number of special events documents above, exhibit PDFs that show there is a decrease in $CH_4$ concentrations the further the distance from CM-A (Figures 12 and 13), indicating that CM-A is consistent with the major $CH_4$ emission sources in these regions. These decreases of $CH_4$ concentrations were observed in terms of the median, mean, distribution width, and percentage over 4.0 ppm all decreasing from 1 km north to 3 km north and again from 3 km north to 5 km north.
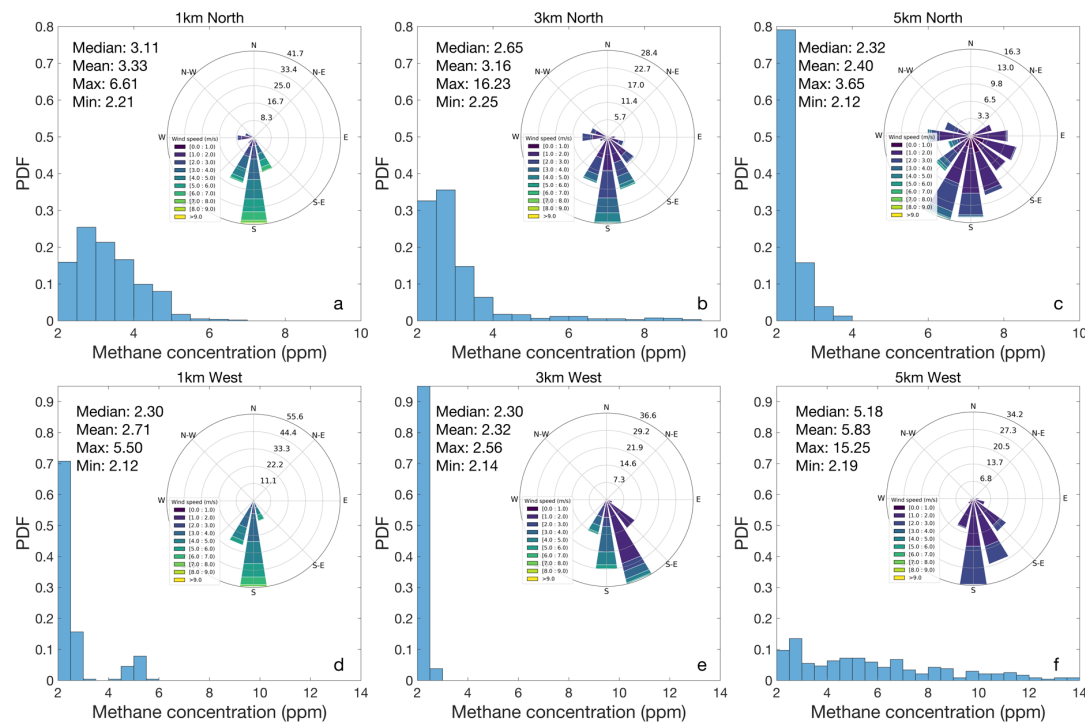
**Figure 12. Probability density map for $CH_4$ concentrations and wind rose measured at 1 km north (a), 1 km west (d), 3 km north (b), 3 km west (e), 5 km north (c), and 5 km west (f) of CM-A and corresponding wind rose chart.**
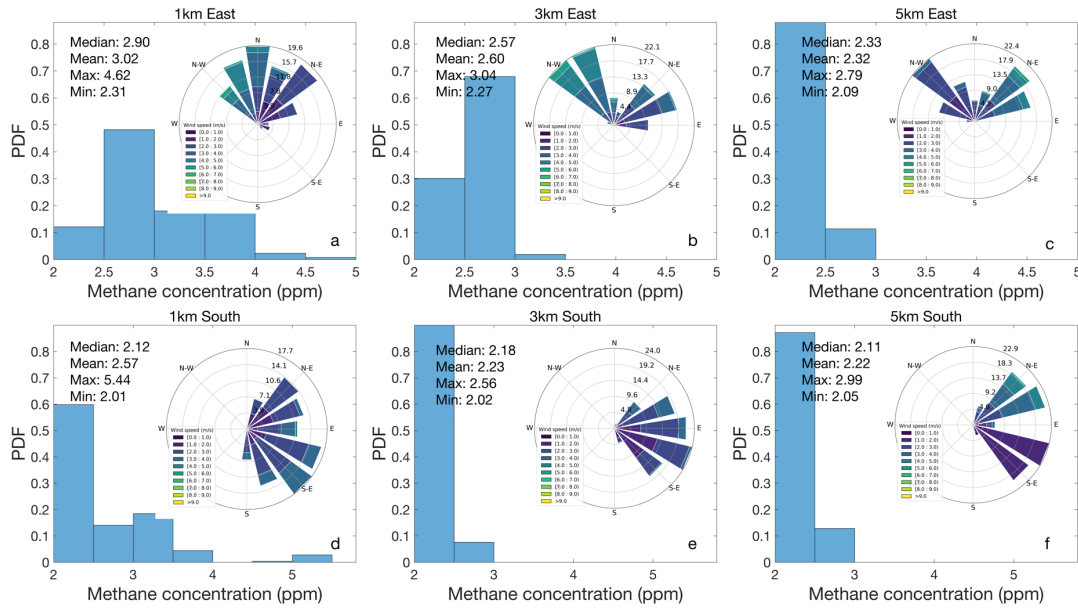
**Figure 13. Probability density map for CH₄ concentrations and wind rose measured at 1 km east (a), 1 km south (d), 3 km east (b), 3 km south (e), 5 km east (c), and 5 km south (f) of CM-A and corresponding wind rose chart.**

The observed CH₄ concentrations gradient as one moves westward from CM-A is inconsistent with the other ordinal directions (Figure 12d, e, f). While there was a small decrease in the mean and distribution breadth from 1 km west to 3 km west, there was a large increase in the median, mean, distribution width, percentatge over 4.0 ppm from 3 km west to 5 km west. Furthermore, the data at 5 km west was found to be skewed differently than at the other sites, with approximately 70% of the CH₄ concentrations data greater than 4.0 ppm. The data clearly indicates that the 5 km west site behaves more like a CH₄ emission source region than even the 1 km north site.

**3.2 Quantification and Emission Characteristics of CMM**

The CH₄ emissions have been estimated at each of the observation poits, with 25.7% of CH₄ concentrations observations yielding emissions results. The PDFs of the CH₄ emissions (Figures 14 and 15) reveal that the three stations in the north and the 5 km west station all are relatively high and variable, while the remainder are relatively low and non-variable. Among all the CH₄ emissions results, the highest median, mean, maximum, and breadth of the distribution are all observed at 5 km west. Another, The 3 km south location has the lowest CH₄ emissions of all points observed (by median), with a respective median, mean, maximum, and percentage greater than 1.0 ppm min$^{-1}$ of (0.03 ppm min$^{-1}$, 0.26 ppm min$^{-1}$, 0.90 ppm min$^{-1}$, 0%) (Figure 15), and is

 subsequently considered representative of $CH_4$ background emissions in this work. It

 is important to note that there is no area within this region that has 0 ppm min$^{-1}$

 emissions and that the minimum $CH_4$ concentration on average is about 2.23 ppm

 (Figure 13), both of which are considered very high or polluted compared with most

 other current studies (Irakulis-Loitxate et al., 2021; Sadavarte et al., 2021).

429
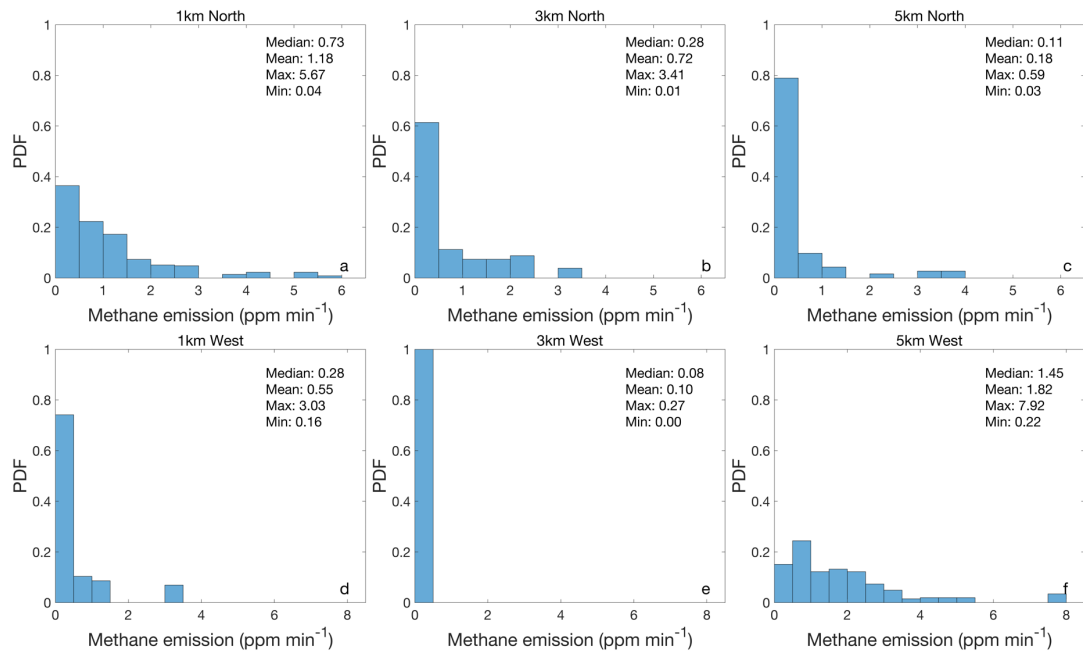
**Figure 14. Probability density functions (PDF) of $CH_4$ emissions located at 1 km north (a), 3 km north (b), 5 km north (c), 1 km west (d), 3 km west (e), and 5 km west (f) of CM-A, including median, mean, maximum, and minimum statistics.**

433
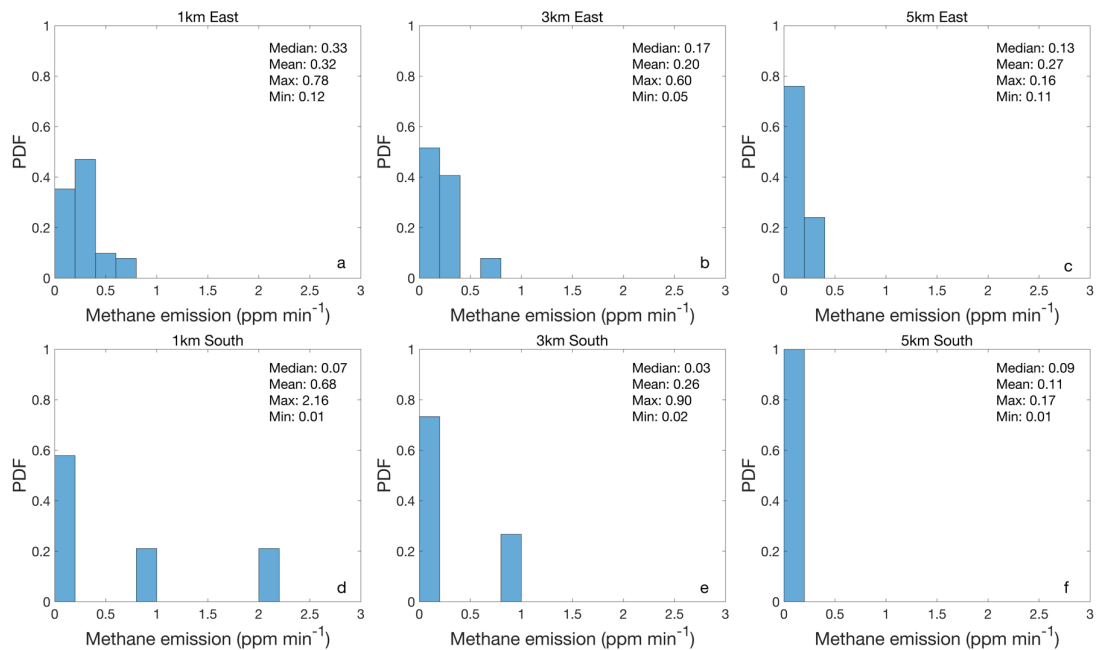
**Figure 15. Probability density functions (PDF) of $CH_4$ emissions located at 1 km east (a), 3 km east (b), 5 km east (c), 1 km south (d), 3 km south (e), and 5 km south (f) of CM-A, including median, mean, maximum, and**

436 **minimum statistics.**

437    The spatial distribution characteristics of the $CH_4$ emissions is similar to that of

438 the $CH_4$ concentrations observations (Figure 14). First, there is a decrease as

439 observation ponts moves northward along the axis away from CM-A, with the median,

440 mean, maximum, and percentage of emissions greater than 1.0 ppm min$^{-1}$ at 1 km north

441 (0.73 ppm min$^{-1}$, 1.18 ppm min$^{-1}$, 5.67 ppm min$^{-1}$, and 42%) all larger than at 3km north

442 (0.28 ppm min$^{-1}$, 0.72 ppm min$^{-1}$, 3.41 ppm min$^{-1}$, and 29%). The $CH_4$ emissions values

443 at 3 km north are also larger than those at 5 km north, which respectively are 0.11 ppm

444 min$^{-1}$, 0.18 ppm min$^{-1}$, and 0.59 ppm min$^{-1}$, and 0%. The subset of $CH_4$ emissions under

445 low wind speed conditions exhibited a larger decline from 1 km to 3 km and from 3 km

446 to 5 km. The observations are further consistent with transport from a single dominant

447 source located at CM-A being the primary driving factor, and diffusion from other

448 industrial sources in Changzhi city center being a secondary factor.

449    Consistent with there being few to no sources impacting the 1 km west and 3 km

450 west sites, except for considerably less transport from CM-A the $CH_4$ emissions PDFs

451 at these sites (Figure 14) demonstrate low $CH_4$ emissions and low variability, with the

452 respective median, mean, maximum, and percentage of $CH_4$ emissions greater than 1.0

453 ppm min$^{-1}$ at 1 km west being  0.28 ppm min$^{-1}$, 0.55 ppm min$^{-1}$ , 3.03 ppm min$^{-1}$, and

454 16% and at 3km west being even lower (0.08 ppm min$^{-1}$, 0.10 ppm min$^{-1}$, 0.27 ppm

455 min$^{-1}$, and 0%). However, the $CH_4$ emissions values at 5 km west were the highest and

456 most variable of all results in this work, with the respective statistics being 1.45 ppm

457 min$^{-1}$, 1.82 ppm min$^{-1}$, 7.92 ppm min$^{-1}$, and 60%. Furthermore, the skewness of the

458 distribution at 5 km west (which has 30% of the $CH_4$ emissions above 2.0 ppm min$^{-1}$)

459 is much larger than at 1 km north (which only has 15% of emissions above 2.0 ppm

460 min$^{-1}$). Combining these pieces of information, at first look it seems that the site at 5

461 km west is not related to the $CH_4$ emissions from CM-A, or at best are a mixture of $CH_4$

462 emissions from CM-A and those at another site, herein proposed to be CM-B. The

463 remainder of this study focuses on disentangling and attributing contributions from

464 CM-A and CM-B at 5 km west, with the observations at the remaining sites ruled out

465 in terms of having a contribution from CM-B.

**3.3 Attribution of CH₄ Emissions**

This works applied the 2-box model at the 5 km west site and quantified the contribution of both CM-A and CM-B $CH_4$ emissions to the observed $CH_4$ concentration distributions as given in Figure 16. First, the results of the 2-box model produce $CH_4$ concentrations PDFs which overlap with the overall observed $CH_4$ concentrations PDF, indicating that the results are reasonable. Second, space of the $CH_4$ emissions from the two different two coal mines do not overlap, and cover two independent portions of the observed $CH_4$ concentrations PDF. Specifically, the 30%, 50%, and 70% values of $CH_4$ concentrations observed at 5km west are 3.68 ppm, 5.18 ppm, and 6.86 ppm respectively. The $CH_4$ emissions from CM-A yield a $CH_4$ concentration less than 4 ppm most of the time, with a 30%, 50%, 70%, and maximum concentration of 2.96 ppm, 3.15 ppm, 3.31 ppm, and 4.60 ppm, while the $CH_4$ emissions from CM-B yield a $CH_4$ concentration more than 5 ppm most of the time, with a minimum, 30%, 50%, 70%, and maximum concentration of 4.76 ppm, 5.20 ppm, 5.68 ppm, and 6.18 ppm.

Overall, the $CH_4$ emissions from CM-B cover well the observed $CH_4$ concentration values from the range of 50% to 70%, with a single high value around the 90% value, while the $CH_4$ emissions from CM-A cover well the observed $CH_4$ concentration values in the range from 10% to 30%. One weakness is that the length of observation time is not as comprehensive as at the other observation sites, and therefore it is possible that had more observation time been made, the $CH_4$ contributions from CM-B would have filled more of the space between the 70% and 90% levels, and some combination of sources from CM-A and CM-B would have better filled the space between the 30% and 50% levels. The results indicate to a high degree of certainty that the effect of $CH_4$ emissions from the two respective coal mines on $CH_4$ concentrations at west 5 km are distinct, with CM-A the source of emissions in the lower range of the $CH_4$ concentration distribution and CM-B the source for emissions in the higher $CH_4$ concentration range, covering values in the middle and upper range. Improvements in modeling, additional observations, considering possible contributions from additional missing sources, and consideration of longer-range transport could add further improvement and better

496    explore the intermediate range of observed concentrations.
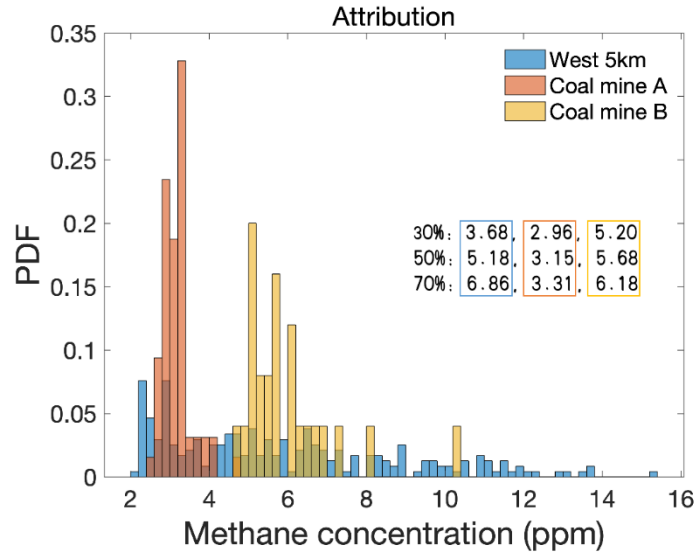
497

498    **Figure 16. Probability density functions (PDF) of CH₄ concentrations (a) observed at the wet 5km site (blue),**

499    **and concetrations simulated by the 2-box model resulting from emissions attributed to (b) Coal mine A (red),**

500    **and (c) Coal mine B (orange). The respective 30th, 50th, and 70th percentiles of the distributions are given in**

501    **text, outlined by the corresponding color box.**

502    **3.4 Policy-Relevant Emissions**

503    In order to compare the values of CH₄ emissions from the Shanxi coal mines computed

504    in section 2.7,   the units (ppm min⁻¹) are transformed into units of (kg h⁻¹) via a

505    conversion factor based on equations (7) and (8). This conversion increases the overall

506    uncertainty, since since it involves approximations of the area swept, the boundary layer

507    height, and and other uncertainties. In this study, average CH₄ emissions from CM-A

508    and CM-B are 6860±3520 kg h⁻¹ and 1010±347 kg h⁻¹, and the CH₄ emissions range is

509    from 102 kg hr⁻¹ to 19000 kg h⁻¹ and 185 kg hr⁻¹ to 1720 kg h⁻¹ repectivily (Table2).

510    Both mines display a fat tail distribution, with respective 25th, median, and 75th

511    percentile values of [1600, 3070, 10500] kg h⁻¹ and [755, 1086, 1416] kg h⁻¹ respectively.

512    These findings are demonstrated to be higher than CH₄ emissions from equivalent oil

513    and gas operations in the USA (Chen et al., 2022), with one site being roughly double

514    and the other similar to and slightly lower than day-to-day emissions inverted over 5-

515    years from TROPOMI (Hu et al., 2024) over the same region. This is consistent with

516    the fact that the results herein target very high frequency and spatially confined

517    emissions, while satellites provide day-to-day values over a larger pixel area, as well as

518    associated significant uncertainties involved in converting from ppm to kg. In specific,

at CM-A, the minimum value (102 kg h$^{-1}$) of CH$_4$ emissions is greater than the minimum value (8 kg h$^{-1}$) of CH$_4$ emissions inverted from TROPOMI, the maxmum value (19.0 ton h$^{-1}$) of CH$_4$ emissions is less than the maximum value (24.9 ton h$^{-1}$) of CH$_4$ emissions from TROPOMI. Similarly, at CM-B, the minimum value (185 kg h$^{-1}$) of CH$_4$ emissions is greater than the minimum value (20 kg h$^{-1}$) of CH$_4$ emissions inverted from TROPOMI, the maxmum value (1720 kg h$^{-1}$) of CH$_4$ emissions is much smaller than the maximum value (37.3 ton h$^{-1}$) of CH$_4$ emissions from TROPOMI. In this study, observations were made within 1km of the coal mines on a minute-to-minute basis, while the TROPOMI observed the XCH$_4$ over a space scale (5.5×7 km$^2$) and on a day-to-day average basis, the higher temporal resolution of our in-situ measurements offers an advantage in capturing short-term variations and extreme values within the study period when compared with TROPOMI's results, due to both the fat-tail distribution and the strong temporal variation of the observations. For this reason, it is likely that the sampling time (two days) at CM-B was insufficient to fully capture the fat tail of the CH$_4$ emissions. The estimation of CH$_4$ emissions from coal mine B in this study carries multiple sources of uncertainty. First, the site has a smaller amount of data than the other sites, and therefore may be less statistically representative. Second, the site generally has a lower production level and is thought to have a lower emission, however, its method of venting is also not known and there could be other such reasons why it could have very variable emissions over time. Third, the TROPOMI emissions themselves are occurring on different grids, which have different properties in terms of surface albedo, aerosols, and other factors, and therefore will be more uncertain at site B than site A, since site A was constrained using ground-trothed data. Finally, there likely are additional sources in the same upwind regions and direction, but further from the observations than site B, which would require additional measurements in the other three ordinal directions from site B to further disentangle. More accurate CH$_4$ emission would require additional monitoring data over a longer time, as well as in the other three ordinal directions around site B. Furthermore, coal mine B has a relatively small coal production compared to coal mine A. Given that coal mine B is only about 6 km away from coal mine A and shares the same geological environment, its CH$_4$ emissions

549 should theoretically be lower than those from coal mine A, but only assuming if the

550 ventilation technology and work schedules were consistent with each other, for which

551 we have no a priori information.

552

553 **Table 2. The $CH_4$ emissions (kg h$^{-1}$) of CM-A and CM-B using different observation methods and statistical**

554 **methods, H means the hight.**

| Coal mines | High frequency ground observation $CH_4$ emissions (kg h$^{-1}$) | | | | | | | | TROPOMI inverted $CH_4$ emissions (kg h$^{-1}$) | | | |
|---|---|---|---|---|---|---|---|---|---|---|---|---|
| | H: Lowest boundary layer | | | | H: Vertical wind×time | | | | | | | |
| | Mean±SE | Min | Median | Max | Mean±SE | Min | Median | Max | Mean±SE | Min | Median | Max |
| CM-A | 6860±3520 | 102 | 3070 | 19000 | 8200±4400 | 67 | 3160 | 22800 | 5500±700 | 8 | 2130 | 24900 |
| CM-B | 1010±347 | 185 | 1090 | 1720 | 200±65 | 34 | 211 | 337 | 6200±1000 | 20 | 1450 | 37300 |

## 4 Conclusions

555

556 This study presents a high frequency ground observation campaign and a new

557 analytical top down emissions estimation approach to quantify the emissions of $CH_4$

558 from a high gas coal mine region with multiple mines. The base observations are made

559 using a portable greenhouse gas analyzer in connection with meterological and other

560 optical measurements. Observations have been made over 15 days at a frequency of 1

561 Hz, at various locations of known distance from an existing high production coal mine.

562 The high frequency observations are then used in connection with a mass conserving

563 modeling platform to estimate the $CH_4$ emissions rate. A mass-conserving Two-Box

564 model was used for attribution analysis in this study. The results show that the spatial

565 characteristics of $CH_4$ concentration/emissions are consistent with the distance from a

566 well characterized of single coal mine within 5km distance, and $CH_4$ emissions

567 demonstrate clear first order effects of both transport and diffusion, with $CH_4$ emission

568 rates of 0.73, 0.28 and 0.15 ppm min$^{-1}$ at 1, 3 and 5 km downwind respectively. At 5

569 km north the overall $CH_4$ concentration (2.40±0.28 ppm) was generally lower than at

570 3km and had much lower variability, consistent with background $CH_4$, which

571 demonstrate that the CMM emissions mainl affect the surrounding area within 5 km

572 distance. However, the overlap of two coal mines (CM-A and CM-B) have a far more

573 complex distribution of $CH_4$ emissions intensity, ranging as high as 1.82 ppm min$^{-1}$,

574 which is much higher than the emissions of single source at any directions. Another, the

background concentration of surface $CH_4$ in the mining areas is very high compared with other studies, with a value always at and above 2.23 ppm. Finally, in order to compare these results with results from other parts of the world, the subset of emissions which successfully underwent attribution were converted into the unit of kg h$^{-1}$ using an approximation of the volume swept by the wind and other approximations of the atmosphere. The resulting values were found to be 6860±3520 kg h$^{-1}$ and 1010±347 kg h$^{-1}$ respectively, which are higher than $CH_4$ emissions from equivalent oil and gas operations in the USA, and in one case are higher than but in the other case similar to day-to-day emissions inverted from 5-years of TROPOMI over the same region.

This work demonstrates that high frequency surface observations of $CH_4$, in combination with high frequency observations of wind can provide deep insights into emissions by accounting for high frequency changes in space and time at the same time, which tend to be missing from models which used more idealized approaches (such as average plume shapes and sizes, levels of coal production, and interpreting gradients from a small number of fixed images). A significant source of $CH_4$ emissions from a previously unknown or improperly classified mine may pose a vastly different range of observed concentration as well as computed emissions than expected. The importance of observations at both high frequency and regional spatial coverage are demonstrated, and a set of practical methods that are freely open and can be adopted and modified rapidly are provided. The approach to source attribution used herein can provide insights to policymakers to formulate regional emission control policies and provide a check on or a priori assumption for the new generation of advance satellite-based top-down emissions estimates, while demonstrating that spatial attribution is a critical next-step for satellite approximations and $CH_4$ control policies.

**Data Availability.** All underlying data herein are available for access by the editors and reviewers at https://figshare.com/s/1a393772d7b72ae17e62 and will be made available to the community upon publication.

**Author contributions.** K.Q., J.B.C. and F.L. designed the research; F.L., C.Y., and Y.S. collected the data; J.B.C. and F.L. analyzed the data; Q.T., W. H. and Q.X. provided the support for data analysis and drawing; Q.H., S.W gave suggestion on running the 2-Box model; F.L. wrote the manuscript with

inputs from J.B.C., Q.H. and P.T.; All authors discussed the results and contributed to the final manuscript.

**Competing interests.** The authors declare that they have no known competing financial interests or personal relationships that could have appeared to influence the work reported in this paper.

**Disclaimer.** Publisher's note: Copernicus Publications remains neutral with regard to jurisdictional claims made in the text, pub- lished maps, institutional affiliations, or any other geographical representation in this paper. While Copernicus Publications makes ev- ery effort to include appropriate place names, the final responsibility lies with the authors.

**Acknowledgments.** We sincerely appreciate all the scientists, engineers, and students who participated in the field campaigns, maintained the measurement instruments, and helped with and collection and processing of the data.

**Finacial support.** This study was funded by the National Natural Science Foundation of China (42075147, 42375125) and the Fundamental Research Funds for the Central Universities (2023KYJD1003, JP230021).

# References

Allen, D. T.: Methane emissions from natural gas production and use: reconciling bottom-up and top-down measurements, Curr. Opin. Chem., 5, 78-83, https://doi.org/10.1016/j.coche.2014.05.004, 2014.

Bloom, A. A., Bowman, K. W., Lee, M., Turner, A. J., Schroeder, R., Worden, J. R., Weidner, R., McDonald, K. C., and Jacob, D. J.: A global wetland methane emissions and uncertainty dataset for atmospheric chemical transport models (WetCHARTs version 1.0), Geosci. Model Dev., 10, 2141-2156, https://gmd.copernicus.org/articles/10/2141/2017/, 2017.

Bournazian, J.: US. Energy Information Administration, https://hdl.handle.net/1813/4504, 2016.

Brandt, A. R., Heath, G. A., Kort, E. A., O'Sullivan, F., Pétron, G., Jordaan, S. M., Tans, P., Wilcox, J., Gopstein, A. M., Arent, D., Wofsy, S., Brown, N. J., Bradley, R., Stucky, G. D., Eardley, D., and Harriss, R.: Methane Leaks from North American Natural Gas Systems, Science, 343, 733-735, https://www.science.org/doi/abs/10.1126/science.1247045, 2014.

Brantley, H. L., Thoma, E. D., Squier, W. C., Guven, B. B., and Lyon, D.: Assessment of methane emissions from oil and gas production pads using mobile measurements, Environ. Sci. Technol., 48(24), 14508-14515, https://pubs.acs.org/doi/full/10.1021/es503070q, 2014.

Brasseur, G. P., and Jacob, D. J.: Model Equations and Numerical Approaches, in: Modeling of atmospheric chemistry, Cambridge University Press Publishing, 84-91, https://books.google.com.hk/books, 2017.

Bruno, J. H., Jervis, D., Varon, D. J., and Jacob, D. J.: U-Plume: automated algorithm for plume detection and source quantification by satellite point-source imagers, Atmos. Meas. Tech., 17, 2625-2636, https://amt.copernicus.org/articles/17/2625/2024/, 2024.

Buchwitz, M., Schneising, O., Reuter, M., Heymann, J., Krautwurst, S., Bovensmann, H., Burrows, J. P., Boesch, H., Parker, R. J., Somkuti, P., Detmers, R. G., Hasekamp, O. P., Aben, I., Butz, A., Frankenberg, C., and Turner, A. J.: Satellite-derived methane hotspot emission estimates using a fast data-driven method, Atmos. Chem. Phys., 17, 5751-5774, https://acp.copernicus.org/articles/17/5751/2017/, 2017.

Butz, A., Galli, A., Hasekamp, O., Landgraf, J., Tol, P., and Aben, I.: TROPOMI aboard Sentinel-5 Precursor: Prospective performance of $CH_4$ retrievals for aerosol and cirrus loaded atmospheres, Remote Sens. Environ., 120, 267-276, https://doi.org/10.1016/j.rse.2011.05.030, 2012.

Cao, X.: Policy and regulatory responses to coalmine closure and coal resources consolidation for sustainability in Shanxi, China, J. Clean. Prod., 145, 199-208, https://doi.org/10.1016/j.jclepro.2017.01.050, 2017.

Chen, Y., Sherwin, E. D., Berman, E. S. F., Jones, B. B., Gordon, M. P., Wetherley, E. B., Kort, E. A., and Brandt, A. R.: Quantifying Regional Methane Emissions in the New Mexico Permian Basin with a Comprehensive Aerial Survey, Environ. Sci. Technol., 56, 4317-4323, https://doi.org/10.1021/acs.est.1c06458, 2022.

Cohen, J. B., and Prinn, R. G.: Development of a fast, urban chemistry metamodel for inclusion in global models, Atmos. Chem. Phys., 11, 7629-7656, https://acp.copernicus.org/articles/11/7629/2011/, 2011.

Cohen, J. B., and Wang, C.: Estimating global black carbon emissions using a top-down Kalman Filter approach, J. Geophys Res: Atmos., 119, 307-323, https://doi.org/10.1002/2013JD019912, 2014.

Conrad, B. M., Tyner, D. R., and Johnson, M. R.: Robust probabilities of detection and quantification uncertainty for aerial methane detection: Examples for three airborne technologies. Remote Sens. Environ., 288, 113499, https://doi.org/10.1016/j.rse.2023.113499, 2023.

Delkash, M., Zhou, B., Han, B., Chow, F. K., Rella, C. W., and Imhoff, P. T.: Short-term landfill methane emissions dependency on wind, Waste Management, 55, 288-298, https://doi.org/10.1016/j.wasman.2016.02.009, 2016.

Duren, R. M., Thorpe, A. K., Foster, K. T., Rafiq, T., Hopkins, F. M., Yadav, V., Bue, B. D., Thompson, D. R., Conley, S., Colombi, N. K., Frankenberg, C., McCubbin, I. B., Eastwood, M. L., Falk, M., Herner, J. D., Croes, B. E., Green, R. O., and Miller, C. E.: California's methane super-emitters, Nature, 575, 180-184, https://doi.org/10.1038/s41586-019-1720-3, 2019.

Etminan, M., Myhre, G., Highwood, E. J., and Shine, K. P.: Radiative forcing of carbon dioxide, methane, and nitrous oxide: A significant revision of the methane radiative forcing, Geophys. Res. Lett., 43, 12614-12623, https://doi.org/10.1002/2016GL071930, 2016.

Goldsmith, C. D., Chanton, J., Abichou, T., Swan, N., Green, R., and Hater, G.: Methane emissions from 20 landfills across the United States using vertical radial plume mapping, J. Air Waste Manage., 62, 183-197, https://doi.org/10.1080/10473289.2011.639480, 2012.

Gorchov Negron, A. M., Kort, E. A., Conley, S. A., and Smith, M. L.: Airborne Assessment of Methane Emissions from Offshore Platforms in the U.S. Gulf of Mexico, Environ. Sci.Technol., 54, 5112-5120, https://doi.org/10.1021/acs.est.0c00179, 2020.

Guo, J., Zhang, J., Shao, J., Chen, T., Bai, K., Sun, Y., Li, N., Wu, J., Li, R., Li, J., Guo, Q., Cohen, J. B., Zhai, P., Xu, X., and Hu, F.: A merged continental planetary boundary layer height dataset based on high-resolution radiosonde measurements, ERA5 reanalysis, and GLDAS: Earth Syst. Sci. Data, v. 16, no. 1, p. 1-14. https://essd.copernicus.org/articles/16/1/2024/essd-16-1-2024.html, 2024.

Heerah, S., Frausto-Vicencio, I., Jeong, S., Marklein, A. R., Ding, Y., Meyer, A. G., Parker, H. A., Fischer, M. L., Franklin, J. E., Hopkins, F. M., and Dubey, M.: Dairy Methane Emissions in California's San Joaquin Valley Inferred With Ground-Based Remote Sensing Observations in the Summer and Winter, Journal of Geophys Res: Atmo., 126, e2021JD034785, https://doi.org/10.1029/2021JD034785, 2021.

He, T.-L., Boyd, R. J., Varon, D. J., and Turner, A. J.: Increased methane emissions from oil and gas following the Soviet Union's collapse, PNAS, 121, e2314600121, https://doi.org/10.1073/pnas.2314600121, 2024.

Hiller, R. V., Neininger, B., Brunner, D., Gerbig, C., Bretscher, D., Künzle, T., Buchmann, N., and Eugster, W.: Aircraft-based $CH_4$ flux estimates for validation of emissions from an agriculturally dominated area in Switzerland, Journal of Geophys Res: Atmos., 119, 4874-4887,

https://doi.org/10.1002/2013JD020918, 2014.

Hu, H., Landgraf, J., Detmers, R., Borsdorff, T., Aan de Brugh, J., Aben, I., Butz, A., and Hasekamp, O.: Toward Global Mapping of Methane With TROPOMI: First Results and Intersatellite Comparison to GOSAT, Geophys. Res. Lett., 45, 3682-3689, https://doi.org/10.1002/2018GL077259, 2018.

Irakulis-Loitxate, I., Guanter, L., Liu, Y.-N., Varon, D. J., Maasakkers, J. D., Zhang, Y., Chulakadabba, A., Wofsy, S. C., Thorpe, A. K., Duren, R. M., Frankenberg, C., Lyon, D. R., Hmiel, B., Cusworth, D. H., Zhang, Y., Segl, K., Gorroño, J., Sánchez-García, E., Sulprizio, M. P., Cao, K., Zhu, H., Liang, J., Li, X., Aben, I., and Jacob, D. J.: Satellite-based survey of extreme methane emissions in the Permian basin, Sci. Adv., 7, eabf4507, https://www.science.org/doi/abs/10.1126/sciadv.abf4507, 2021.

Jacob, D. J., Turner, A. J., Maasakkers, J. D., Sheng, J., Sun, K., Liu, X., Chance, K., Aben, I., McKeever, J., and Frankenberg, C.: Satellite observations of atmospheric methane and their value for quantifying methane emissions, Atmos. Chem. Phys., 16, 14371-14396, https://acp.copernicus.org/articles/16/14371/2016/, 2016.

Jacob, D. J., Varon, D. J., Cusworth, D. H., Dennison, P. E., Frankenberg, C., Gautam, R., Guanter, L., Kelley, J., McKeever, J., Ott, L. E., Poulter, B., Qu, Z., Thorpe, A. K., Worden, J. R., and Duren, R. M.: Quantifying methane emissions from the global scale down to point sources using satellite observations of atmospheric methane, Atmos. Chem. Phys., 22, 9617-9646, https://acp.copernicus.org/articles/22/9617/2022/, 2022.

Janssens-Maenhout, G., Crippa, M., Guizzardi, D., Muntean, M., and Petrescu, A. M. R.: EDGAR v4.3.2 Global Atlas of the three major Greenhouse Gas Emissions for the period 1970–2012, Earth Syst. Sci. Data, 1-55, https://doi.org/10.5194/essd-2017-79, 2017.

Karion, A., Sweeney, C., Pétron, G., Frost, G., Michael Hardesty, R., Kofler, J., Miller, B. R., Newberger, T., Wolter, S., Banta, R., Brewer, A., Dlugokencky, E., Lang, P., Montzka, S. A., Schnell, R., Tans, P., Trainer, M., Zamora, R., and Conley, S.: Methane emissions estimate from airborne measurements over a western United States natural gas field, Geophys. Res. Lett., 40, 4393-4397, https://doi.org/10.1002/grl.50811, 2013.

Katzenstein, A. S., Doezema, L. A., Simpson, I. J., Blake, D. R., and Rowland, F. S.: Extensive regional atmospheric hydrocarbon pollution in the southwestern United States, PNAS, 100, 11975-11979, https://www.pnas.org/doi/abs/10.1073/pnas.1635258100, 2003.

Kerr, T., and Yang, M.: Coal mine methane in China: A budding asset with the potential to bloom, IEA Information Paper, 1-35, https://www.iea.org/reports/coal-mine-methane-in-china-a-budding-asset-with-the-potential-to-bloom, 2009.

Kirschke, S., Bousquet, P., Ciais, P., Saunois, M., Canadell, J. G., Dlugokencky, E. J., Bergamaschi, P., Bergmann, D., Blake, D. R., Bruhwiler, L., Cameron-Smith, P., Castaldi, S., Chevallier, F., Feng, L., Fraser, A., Heimann, M., Hodson, E. L., Houweling, S., Josse, B., Fraser, P. J., Krummel, P. B., Lamarque, J.-F., Langenfelds, R. L., Le Quéré, C., Naik, V., O'Doherty, S., Palmer, P. I., Pison, I., Plummer, D., Poulter, B., Prinn, R. G., Rigby, M., Ringeval, B., Santini, M., Schmidt, M., Shindell, D. T., Simpson, I. J., Spahni, R., Steele, L. P., Strode, S. A., Sudo, K., Szopa, S., van der Werf, G. R., Voulgarakis, A., van Weele, M., Weiss, R. F., Williams, J. E., and Zeng, G.: Three decades of global methane sources and sinks, Nat. Geosci., 6, 813-823, https://doi.org/10.1038/ngeo1955, 2013.

Krautwurst, S., Gerilowski, K., Borchardt, J., Wildmann, N., Gałkowski, M., Swolkień, J., Marshall, J., Fiehn, A., Roiger, A., Ruhtz, T., Gerbig, C., Necki, J., Burrows, J. P., Fix, A., and Bovensmann, H.: Quantification of $CH_4$ coal mining emissions in Upper Silesia by passive airborne remote sensing observations with the Methane Airborne MAPper (MAMAP) instrument during the $CO_2$ and Methane (CoMet) campaign, Atmos. Chem. Phys., 21, 17345-17371, https://acp.copernicus.org/articles/21/17345/2021/, 2021.

Krautwurst, S., Gerilowski, K., Jonsson, H. H., Thompson, D. R., Kolyer, R. W., Iraci, L. T., Thorpe, A. K., Horstjann, M., Eastwood, M., Leifer, I., Vigil, S. A., Krings, T., Borchardt, J., Buchwitz, M., Fladeland, M. M., Burrows, J. P., and Bovensmann, H.: Methane emissions from a Californian landfill, determined from airborne remote sensing and in situ measurements, Atmos. Meas. Tech., 10, 3429-3452, https://amt.copernicus.org/articles/10/3429/2017/, 2017.

Kuhlmann, G., Brunner, D., Emmenegger, L., Schwietzke, S., Zavala-Araiza, D., Thorpe, A., Hueni, A., and Röckmann, T.: Quantifying methane super-emitters from oil and gas production in Romania with the AVIRIS-NG imaging spectrometer, EGU General Assembly 2023, Vienna, Austria., 24–28 Apr 2023 EGU23-6751.

Kuze, A., Suto, H., Nakajima, M., and Hamazaki, T.: Thermal and near infrared sensor for carbon observation Fourier-transform spectrometer on the Greenhouse Gases Observing Satellite for greenhouse gases monitoring, Appl. Optics., 48, 6716-6733, https://opg.optica.org/ao/abstract.cfm?URI=ao-48-35-6716, 2009.

Lauvaux, T., Giron, C., Mazzolini, M., d'Aspremont, A., Duren, R., Cusworth, D., Shindell, D., and Ciais, P.: Global assessment of oil and gas methane ultra-emitters, Science, 375, 557-561, https://www.science.org/doi/abs/10.1126/science.abj4351, 2022.

Li, Q., Fernandez, R. P., Hossaini, R., Iglesias-Suarez, F., Cuevas, C. A., Apel, E. C., Kinnison, D. E., Lamarque, J.-F., and Saiz-Lopez, A.: Reactive halogens increase the global methane lifetime and radiative forcing in the 21st century, Nat. Commun., 13, 2768, https://doi.org/10.1038/s41467-022-30456-8, 2022.

Li, X., Cohen, J. B., Qin, K., Geng, H., Wu, L., Wu, X., Yang, C., Zhang, R., and Zhang, L.: Remotely Sensed and Surface Measurement Derived Mass-Conserving Inversion of Daily High-Resolution NOx Emissions and Inferred Combustion Technologies in Energy Rich Northern China, Atmos. Chem. Phys., 23, 8001-8019, https://egusphere.copernicus.org/preprints/2023/egusphere-2023-2/, 2023,.

Lin, B.-q., and Liu, J.-h.: Estimating coal production peak and trends of coal imports in China, Energ. Policy, 38, 512-519, https://doi.org/10.1016/j.enpol.2009.09.042, 2010.

Lu, L., Cohen, J. B., Qin, K., Li, X., and He, Q.: Identifying Missing Sources and Reducing NOx Emissions Uncertainty over China using Daily Satellite Data and a Mass-Conserving Method, EGUsphere [ACCEPTED], https://doi.org/10.5194/egusphere-2024-1903, 2024.

Luther, A., Kleinschek, R., Scheidweiler, L., Defratyka, S., Stanisavljevic, M., Forstmaier, A., Dandocsi, A., Wolff, S., Dubravica, D., Wildmann, N., Kostinek, J., Jöckel, P., Nickl, A. L., Klausner, T., Hase, F., Frey, M., Chen, J., Dietrich, F., Nęcki, J., Swolkień, J., Fix, A., Roiger, A., and Butz, A.: Quantifying CH4 emissions from hard coal mines using mobile sun-viewing Fourier transform spectrometry, Atmos. Meas. Tech., 12, 5217-5230, https://amt.copernicus.org/articles/12/5217/2019/, 2019.

Luther, A., Kostinek, J., Kleinschek, R., Defratyka, S., Stanisavljević, M., Forstmaier, A., Dandocsi, A., Scheidweiler, L., Dubravica, D., Wildmann, N., Hase, F., Frey, M. M., Chen, J., Dietrich, F., Nęcki, J., Swolkień, J., Knote, C., Vardag, S. N., Roiger, A., and Butz, A.: Observational constraints on methane emissions from Polish coal mines using a ground-based remote sensing network, Atmos. Chem. Phys., 22, 5859-5876, https://acp.copernicus.org/articles/22/5859/2022/, 2022.

Mehrotra, S., Faloona, I., Suard, M., Conley, S., and Fischer, M. L.: Airborne Methane Emission Measurements for Selected Oil and Gas Facilities Across California, Environ. Sci. Technol., 51, 12981-12987, https://doi.org/10.1021/acs.est.7b03254, 2017.

Miller, S. M., Michalak, A. M., Detmers, R. G., Hasekamp, O. P., Bruhwiler, L. M. P., and Schwietzke, S.: China's coal mine methane regulations have not curbed growing emissions, Nat. Commun., 10, 303, https://doi.org/10.1038/s41467-018-07891-7, 2019.

Molina, L. T., Madronich, S., Gaffney, J. S., Apel, E., de Foy, B., Fast, J., Ferrare, R., Herndon, S., Jimenez, J. L., Lamb, B., Osornio-Vargas, A. R., Russell, P., Schauer, J. J., Stevens, P. S., Volkamer, R., and Zavala, M.: An overview of the MILAGRO 2006 Campaign: Mexico City emissions and their transport and transformation, Atmos. Chem. Phys., 10, 8697-8760, https://acp.copernicus.org/articles/10/8697/2010/, 2010.

Peng, S., Piao, S., Bousquet, P., Ciais, P., Li, B., Lin, X., Tao, S., Wang, Z., Zhang, Y., and Zhou, F.: Inventory of anthropogenic methane emissions in mainland China from 1980 to 2010, Atmos. Chem. Phys., 16, 14545-14562, https://acp.copernicus.org/articles/16/14545/2016/, 2016.

Plant, G., Kort, E. A., Murray, L. T., Maasakkers, J. D., and Aben, I.: Evaluating urban methane emissions

from space using TROPOMI methane and carbon monoxide observations, Remote Sen. Environ., 268, 112756, https://doi.org/10.1016/j.rse.2021.112756, 2022.

Povey, A. C., and Grainger, R. G.: Known and unknown unknowns: uncertainty estimation in satellite remote sensing, Atmos. Meas. Tech., 8, 4699-4718, https://amt.copernicus.org/articles/8/4699/2015/, 2015.

Prather, M. J., Holmes, C. D., and Hsu, J.: Reactive greenhouse gas scenarios: Systematic exploration of uncertainties and the role of atmospheric chemistry, Geophys. Res. Lett., 39, L09803, https://doi.org/10.1029/2012GL051440, 2012.

Prinn, R., Cunnold, D., Rasmussen, R., Simmonds, P., Alyea, F., Crawford, A., Fraser, P., and Rosen, R.: Atmospheric Trends in Methylchloroform and the Global Average for the Hydroxyl Radical, Science, 238, 945-950, https://www.science.org/doi/abs/10.1126/science.238.4829.945, 1987.

Qin, K., Hu, W., He, Q., Lu, F., and Cohen, J. B.: Individual Coal Mine Methane Emissions Constrained by Eddy-Covariance Measurements: Low Bias and Missing Sources, EGUsphere, 1-49, https://egusphere.copernicus.org/preprints/2023/egusphere-2023-1210/, 2023a.

Qin, K., Lu, L., Liu, J., He, Q., Shi, J., Deng, W., Wang, S., and Cohen, J. B.: Model-free daily inversion of NOx emissions using TROPOMI (MCMFE-NOx) and its uncertainty: Declining regulated emissions and growth of new sources, Remote Sens. Environ., 295, 113720, https://doi.org/10.1016/j.rse.2023.113720, 2023b.

Reuter, M., Buchwitz, M., Schneising, O., Krautwurst, S., O'Dell, C. W., Richter, A., Bovensmann, H., and Burrows, J. P.: Towards monitoring localized $CO_2$ emissions from space: co-located regional $CO_2$ and $NO_2$ enhancements observed by the OCO-2 and S5P satellites, Atmos. Chem. Phys., 19, 9371-9383, https://acp.copernicus.org/articles/19/9371/2019/, 2019.

Rigby, M., Park, S., Saito, T., Western, L. M., Redington, A. L., Fang, X., Henne, S., Manning, A. J., Prinn, R. G., Dutton, G. S., Fraser, P. J., Ganesan, A. L., Hall, B. D., Harth, C. M., Kim, J., Kim, K. R., Krummel, P. B., Lee, T., Li, S., Liang, Q., Lunt, M. F., Montzka, S. A., Mühle, J., O'Doherty, S., Park, M. K., Reimann, S., Salameh, P. K., Simmonds, P., Tunnicliffe, R. L., Weiss, R. F., Yokouchi, Y., and Young, D.: Increase in CFC-11 emissions from eastern China based on atmospheric observations, Nature, 569, 546-550, https://doi.org/10.1038/s41586-019-1193-4, 2019.

Sadavarte, P., Pandey, S., Maasakkers, J. D., Lorente, A., Borsdorff, T., Denier van der Gon, H., Houweling, S., and Aben, I.: Methane Emissions from Superemitting Coal Mines in Australia Quantified Using TROPOMI Satellite Observations, Environ. Sci. Technol., 55, 16573-16580, https://doi.org/10.1021/acs.est.1c03976, 2021.

Saunois, M., Stavert, A. R., Poulter, B., Bousquet, P., Canadell, J. G., Jackson, R. B., Raymond, P. A., Dlugokencky, E. J., Houweling, S., Patra, P. K., Ciais, P., Arora, V. K., Bastviken, D., Bergamaschi, P., Blake, D. R., Brailsford, G., Bruhwiler, L., Carlson, K. M., Carrol, M., Castaldi, S., Chandra, N., Crevoisier, C., Crill, P. M., Covey, K., Curry, C. L., Etiope, G., Frankenberg, C., Gedney, N., Hegglin, M. I., Höglund-Isaksson, L., Hugelius, G., Ishizawa, M., Ito, A., Janssens-Maenhout, G., Jensen, K. M., Joos, F., Kleinen, T., Krummel, P. B., Langenfelds, R. L., Laruelle, G. G., Liu, L., Machida, T., Maksyutov, S., McDonald, K. C., McNorton, J., Miller, P. A., Melton, J. R., Morino, I., Müller, J., Murguia-Flores, F., Naik, V., Niwa, Y., Noce, S., O'Doherty, S., Parker, R. J., Peng, C., Peng, S., Peters, G. P., Prigent, C., Prinn, R., Ramonet, M., Regnier, P., Riley, W. J., Rosentreter, J. A., Segers, A., Simpson, I. J., Shi, H., Smith, S. J., Steele, L. P., Thornton, B. F., Tian, H., Tohjima, Y., Tubiello, F. N., Tsuruta, A., Viovy, N., Voulgarakis, A., Weber, T. S., van Weele, M., van der Werf, G. R., Weiss, R. F., Worthy, D., Wunch, D., Yin, Y., Yoshida, Y., Zhang, W., Zhang, Z., Zhao, Y., Zheng, B., Zhu, Q., Zhu, Q., and Zhuang, Q.: The Global Methane Budget 2000–2017, Earth Syst. Sci. Data, 12, 1561-1623, https://essd.copernicus.org/articles/12/1561/2020/, 2020a.

Saunois, M., Stavert, A. R., Poulter, B., Bousquet, P., and Zhuang, Q.: The Global Methane Budget 2000–2017, Earth System Science Data, 12, 1561-1623, https://doi.org/10.5194/essd-12-1561-2020, 2020b.

Shi, T., Han, G., Ma, X., Mao, H., Chen, C., Han, Z., Pei, Z., Zhang, H., Li, S., and Gong, W.: Quantifying factory-scale $CO_2/CH_4$ emission based on mobile measurements and EMISSION-PARTITION model: cases in China, Environ. Res. Lett., 18, 034028, https://dx.doi.org/10.1088/1748-9326/acbce7, 2023.

Shi, T., Han, Z., Han, G., Ma, X., Chen, H., Andersen, T., Mao, H., Chen, C., Zhang, H., and Gong, W.: Retrieving $CH_4$-emission rates from coal mine ventilation shafts using UAV-based AirCore observations and the genetic algorithm–interior point penalty function (GA-IPPF) model, Atmos. Chem. Phys., 2, 13881-13896, https://acp.copernicus.org/articles/22/13881/2022/, 2022.

Sun, K.: Derivation of Emissions From Satellite-Observed Column Amounts and Its Application to TROPOMI $NO_2$ and CO Observations, Geophys. Res. Lett. , 49, e2022GL101102, https://doi.org/10.1029/2022GL101102, 2022.

Tong, X., van Heuven, S., Scheeren, B., Kers, B., Hutjes, R., and Chen, H.: Aircraft-Based AirCore Sampling for Estimates of $N_2O$ and $CH_4$ Emissions, Environ. Sci. Technol., 57, 15571-15579, https://doi.org/10.1021/acs.est.3c04932, 2023.

Tu, Q., Hase, F., Schneider, M., García, O., Blumenstock, T., Borsdorff, T., Frey, M., Khosrawi, F., Lorente, A., Alberti, C., Bustos, J. J., Butz, A., Carreño, V., Cuevas, E., Curcoll, R., Diekmann, C. J., Dubravica, D., Ertl, B., Estruch, C., León-Luis, S. F., Marrero, C., Morgui, J. A., Ramos, R., Scharun, C., Schneider, C., Sepúlveda, E., Toledano, C., and Torres, C.: Quantification of $CH_4$ emissions from waste disposal sites near the city of Madrid using ground- and space-based observations of COCCON, TROPOMI and IASI, Atmos. Chem. Phys., 22, 295-317, https://acp.copernicus.org/articles/22/295/2022/, 2022.

Varon, D. J., Jacob, D. J., McKeever, J., Jervis, D., Durak, B. O. A., Xia, Y., and Huang, Y.: Quantifying methane point sources from fine-scale satellite observations of atmospheric methane plumes, Atmos. Meas. Tech., 11, 5673-5686, https://amt.copernicus.org/articles/11/5673/2018/, 2018.

Vaughn, T. L., Bell, C. S., Pickering, C. K., Schwietzke, S., Heath, G. A., Pétron, G., Zimmerle, D. J., Schnell, R. C., and Nummedal, D.: Temporal variability largely explains top-down/bottom-up difference in methane emission estimates from a natural gas production region, PNAS, 115, 11712-11717, https://www.pnas.org/doi/abs/10.1073/pnas.1805687115, 2018.

Vinković, K., Andersen, T., de Vries, M., Kers, B., van Heuven, S., Peters, W., Hensen, A., van den Bulk, P., and Chen, H.: Evaluating the use of an Unmanned Aerial Vehicle (UAV)-based active AirCore system to quantify methane emissions from dairy cows, Sci. Total Environ., 831, 154898, https://doi.org/10.1016/j.scitotenv.2022.154898, 2022.

Wecht, K. J., Jacob, D. J., Sulprizio, M. P., Santoni, G. W., Wofsy, S. C., Parker, R., Bösch, H., and Worden, J.: Spatially resolving methane emissions in California: constraints from the CalNex aircraft campaign and from present (GOSAT, TES) and future (TROPOMI, geostationary) satellite observations, Atmos. Chem. Phys., 14, 8173-8184, https://acp.copernicus.org/articles/14/8173/2014/, 2014.

Zhang, Y., Gautam, R., Pandey, S., Omara, M., Maasakkers, J. D., Sadavarte, P., Lyon, D., Nesser, H., Sulprizio, M. P., Varon, D. J., Zhang, R., Houweling, S., Zavala-Araiza, D., Alvarez, R. A., Lorente, A., Hamburg, S. P., Aben, I., and Jacob, D. J.: Quantifying methane emissions from the largest oil-producing basin in the United States from space, *Sci. Adv.*, 6, eaaz5120, https://www.science.org/doi/abs/10.1126/sciadv.aaz5120, 2020.

Zinchenko, A. V., Paramonova, N. N., Privalov, V. I., and Reshetnikov, A. I.: Estimation of methane emissions in the St. Petersburg, Russia, region: An atmospheric nocturnal boundary layer budget approach, J. Geophys. Res-Atmos., 107, ACH 2-1-ACH 2-11, https://doi.org/10.1029/2001JD001369, 2002.